Transformation of Ferrihydrite to Goethite and the Fate of Plutonium

Enrica Balboni, Kurt F Smith, Liane M Moreau, Tian T Li, Melody Maloubier, Corwin H Booth, Annie B Kersting, Mavrik Zavarin

Plutonium fate during ferrihydrite to goethite recrystallization

Enrica Balboni[1], Kurt F. Smith[2], Liane M. Moreau[2], Tian T. Li[3], Melody Maloubier[4], Corwin H. Booth[2], Annie B. Kersting[1], Mavrik Zavarin[1]*

[1] Glenn T. Seaborg Institute, Physical & Life Sciences Directorate, Lawrence Livermore National Laboratory, P.O. Box 808, Livermore, CA 94550, USA

[2] Chemical Sciences Division, Lawrence Berkeley National Laboratory, Berkeley, CA 94720, USA

[3] Material Science division, Physical & Life Sciences Directorate, Lawrence Livermore National Laboratory, Livermore, CA 94550, USA

[4] Department of Environmental Engineering & Earth Sciences, Clemson University, Clemson, SC, 29634, USA[a]

KEYWORDS: Ferrihydrite, goethite, recrystallization, plutonium, x-ray absorption spectroscopy

[a] Currently at IJCLab (Laboratoire de Physique des des deux infinis Irène Joliot-Curie - UMR 9012)

ABSTRACT

Understanding interactions between plutonium and iron (oxy)hydroxide minerals is necessary to gain a predictive understanding of plutonium environmental mobility and ensuring long-term performance of nuclear waste repositories. Plutonium sorption and desorption reactions with mineral surfaces, formation of PuO_2 nanoparticles, and coprecipitation processes are all likely important processes under a range of geochemical conditions. We investigated plutonium fate during the formation of ferrihydrite and its subsequent recrystallization to goethite. Ferrihydrite was synthesized with varying quantities of Pu(IV) following either a sorption or coprecipitation process; the ferrihydrite was then aged hydrothermally to yield goethite. The synthesized materials were characterized via extended x-ray absorption fine structure spectroscopy, transmission electron microscopy, and acid leaching to elucidate the nature of plutonium association with ferrihydrite and goethite. In samples prepared following the sorption method, plutonium was identified in two different forms: a PuO_2 precipitate and a surface sorbed plutonium complex. For the samples prepared via coprecipitation the data demonstrate that no PuO_2 formation occurs in the ferrihydrite precursor and in the goethite experiments where plutonium concentration is ≤ 1000 ppm (mg Kg^{-1}). In these coprecipitation experiments plutonium extended x-ray absorption fine structure data indicate the plutonium is strongly bound to the minerals either via formation of a strong inner sphere complex, or via an incorporation process. In the coprecipitation experiments, PuO_2 formation only occurs at the highest plutonium concentration (3000 ppm), suggesting that during ferrihydrite recrystallization part of the plutonium can be remobilized to form PuO_2 nanoparticles if the plutonium concentration is sufficiently elevated. In a series of acid leaching

experiments, less plutonium was removed from the goethite surface when formed via the coprecipitation process compared to the sorption process. Collectively, our results demonstrate that the nature of plutonium associated with the precursor ferrihydrite (adsorbed versus coprecipitated) will have a direct impact on the association of plutonium with its recrystallization product (goethite). Furthermore, the data illustrate that some properties of plutonium association with the precursor ferrihydrite are retained through recrystallization process to goethite. These findings show that plutonium strongly associates to iron (oxy)hydroxides formed through coprecipitation processes and in these materials plutonium can be strongly retained by the iron minerals.

Introduction

The production and testing of nuclear weapons, nuclear accidents, and authorized discharges of radioactive effluents have contributed significantly to plutonium (Pu) contamination in the natural environment. Pu is also a major constituent in civil and military nuclear wastes and is considered a risk-driving radionuclide in the long-term safety of nuclear waste repositories. Due to its long half-life (^{239}Pu t½ =24,100 years) and radiotoxicity, understanding the mobility of Pu in the environment is a key scientific and societal concern.

Several factors can influence Pu mobility in the environment including: Pu redox processes, [1-3] solubility effects, [4, 5] interactions with natural organic matter (including bacteria), [6, 7] and sorption/desorption reactions with mineral surfaces. [8-10] Under typical environmental conditions Pu may exist in the III, IV, V and VI oxidation states, each of which demonstrate dramatically different chemical properties. [11, 12] For example, under environmental conditions the higher oxidation states, V and VI, exist as the highly soluble and mobile PuO_2^{x+} moieties. Pu(IV), which

has a lower solubility than Pu(V) or Pu(VI) in circumneutral environments, can undergo hydrolysis forming Pu polymers at high concentrations. Polymerization reactions may occur at Pu(IV) concentrations > 10^{-8} M [13] and result in the formation of discrete Pu(IV)O_2 intrinsic colloids. [14] Although Pu(IV) and Pu(V) are the most common oxidation states under circumneutral pH conditions, and both sorb to Pu mineral surfaces, Pu(V) has been shown to reduce to Pu(IV) on surfaces. [2, 8, 11, 15-18] Moreover, Pu(IV) has a particularly high affinity for iron (oxy)hydroxides mineral surfaces. [19-21] Iron (oxy)hydroxides are a common constituent of soils, and predominantly form as a weathering product of iron-bearing minerals. [22] In the deep subsurface iron (oxy)hydroxides may form due to biological oxidation of Fe(II) under reducing conditions. [23] Fe minerals in transient and dynamic (bio)geochemical settings such as sediment deposition in lakes or ponds [24-27], will likely be subject to dissolution and recrystallization reactions [19, 20, 28, 29], and the fate of sorbed species during mineral recrystallization is currently unknown. In nuclear repositories planned by several countries the first technical barrier planned for use consist of stainless-steel canisters. [30-32] Under nuclear repositories conditions the steel cask is expected to corrode over the geological timescales considered [30-32] and depending on the engineered backfill material, the natural bedrock, and the nature of surrounding groundwater, a range of Fe minerals may form during the corrosion process. [33, 34]

Ferrihydrite ($Fe_{9.74}O_{14}(OH)_2$)[35] is a poorly crystalline and metastable early product of both biotic and abiotic precipitation of iron, and is a precursor to more crystalline iron oxide phases such as hematite (α-Fe_2O_3) and goethite (α-FeOOH). The hematite and goethite formation processes begin with ferrihydrite particle aggregation [36], followed by recrystallization within the aggregate via dissolution and reprecipitation processes that occur at the nanoscale. [37] Ferrihydrite recrystallization to either hematite or goethite is strongly dependent upon solution conditions,

including pH, ionic strength, and temperature. [38, 39] Ferrihydrite typically exhibits a high surface area with a high capacity to adsorb dissolved metal species [40-42], including U, Np, and Pu. [22, 43-46] These traits of ferrihydrite have been utilized to decontaminate radioactive effluent [47] and in various nuclear abatement technologies. [48]

When Pu is present in solutions where iron (oxy)hydroxide minerals may be forming, such as in a contaminated ponds, lakes, or streams, or during corrosion of steel, its fate is unknown. The Pu could conceivably adsorb to the newly formed iron oxides (e.g. hematite or goethite), be structurally incorporated into the new phases, or be excluded from the newly formed crystal structure due to crystal-chemical constraints. These three different scenarios have vastly different implications for predicting contaminant transport. Smith et. al [43] demonstrated that under high pH conditions (pH 9), Pu forms an inner-sphere tetradentate complex on the ferrihydrite surface [43] which remains unchanged during recrystallization to hematite, suggesting that Pu remains strongly adsorbed to the iron (oxy)hydroxide surface [43] during hematite crystallization. Recent experiments by Marshall et al. (2014) [22] and Bots et al. (2016) [44] showed that U(VI) and Np(V) initially adsorbed to ferrihydrite can be incorporated into a distorted Fe(III) octahedral site in the hematite structure during recrystallization processes. [22,44] The transformation of ferrihydrite to nanoparticulate iron (oxy)hydroxide minerals in the presence of U(VI) resulted in the preferential incorporation of U into goethite (α-FeOOH) over lepidocrocite (γ-FeOOH). [49] At high Pu concentrations (> 10^{-8} M) Pu(IV) intrinsic colloids have been shown to form on the surface of various oxide minerals including iron oxy(hydroxide) minerals. [14, 20, 50, 51] On the goethite surface Pu(IV) colloids may undergo a lattice distortion, due to epitaxial growth, which leads to a stronger surface binding compared to other mineral phases, such as quartz. [52] Both the sorption/desorption of Pu to mineral colloid surfaces (pseudocolloids) and formation of Pu oxide colloids (intrinsic

colloids) associated with mineral surfaces, as well as Pu coprecipitation with secondary minerals are all likely important environmental processes under a range of geochemical conditions.[11, 13, 17, 53, 54] For example in groundwater at the Mayak site (Russia) colloidal amorphous iron oxides with associated Pu were found up to 4 km away from the contamination source. [55] In contaminated Los Alamos National Laboratory, N.M. Batuk et al.[56] identified unusual Pu-Fe particles. The authors suggest that the formation of these particles could have resulted from transitory local chemical conditions from the original waste stream. [56] Finally, Lukashenko et al. (2020) [57] identified particles of Fe-Mn oxides in bottom sediments of streams flowing from the tunnels in the Degelen Mountain, site of USSR nuclear weapon test program. [57] Analysis of the particles indicate that these materials may be formed as secondary minerals, suggesting that their formation is most likely related to sorption and coprecipitation of transuranic elements with oxides and hydroxides of iron and manganese. [57]

The fate of radionuclides, including Pu, during mineral formation and recrystallization processes is still not fully understood. Gaining a detailed, mechanistic, understanding of the interactions between iron (oxy)hydroxides and Pu is key to predicting the long-term stability and mobility of Pu in the natural and engineered environment. The goal of this work is to assess the fate of Pu during the ubiquitous process of ferrihydrite to goethite recrystallization. We synthesized ferrihydrite with various amounts of Pu(IV) following either a coprecipitation or sorption process, and then subsequently used this material to crystallize goethite. We provide a detailed extended x-ray absorption fine structure spectroscopy and transmission electron microscopy characterization of the synthesized minerals and show that the nature of Pu associated with the precursor ferrihydrite (adsorbed versus coprecipitated) will impact the association of Pu with the ferrihydrite recrystallization product (goethite).

Methods

Preparation of Pu stock

A ^{242}Pu stock (99.8% ^{242}Pu, 0.12% ^{240}Pu, 0.005% ^{239}Pu, 0.005% ^{238}Pu by activity) was purified using an anion exchange resin (BioRad AG1-X8, 100–200 mesh). Prior to loading on the resin, Pu was reacted with $NaNO_2$ to convert Pu to Pu(IV). Pu was loaded onto the column in 8 mol/L HNO_3 and the column was subsequently washed with three column volumes of 8 mol/L HNO_3. Pu was stripped from the column using 1 mol/L HCl. The oxidation state of the Pu was determined using the lanthanum fluoride precipitation method [58] and determined to be 97% Pu(III/IV). UV-VIS confirmed that the Pu stock solution was > 95% Pu(IV). The concentration of the purified stock solution was determined by liquid scintillation counting (LSC; Packard Tri-Carb TR2900 LSA) with final concentration of $1.3 \pm 0.1 \times 10^{-3}$ mol/L.

Mineral synthesis

Ferrihydrite *sorption method*: Ferrihydrite (FH) precipitation was induced by drop wise addition of 1-5 mol/L KOH into a 25 mL 0.04 mol/L $FeNO_3.9H_2O$ solution in 30 mL Savillex® PFA (perfluoroalkoxy alkane) vials to yield a final pH ~8. Desired aliquots of a Pu(IV) stock solution were added to the mineral slurries. After addition of the Pu(IV) stock, the pH of the slurries was checked and re-adjusted to the desired value using 1-5 mol/L KOH. The FH-Pu(IV) suspensions were equilibrated for 2 hours. Samples prepared following this sorption method with 3000, 1000, and 400 ppm Pu(IV) will be referred to as FH-S-3000, FH-S-1000, and FH-S-400, respectively.

Ferrihydrite *coprecipitation method*: A 25 mL 0.04 mol/L $FeNO_3.9H_2O$ solution was mixed with desired concentrations of Pu(IV). The solutions were equilibrated for two hours in 30 mL Savillex® PFA vials. Ferrihydrite precipitation was induced by drop wise addition of 1-5 mol/L

KOH to a final pH of ~8 and samples with 3000, 1000, and 400 ppm Pu(IV) will be referred to as FH-C-3000, FH-C-1000, and FH-C-400 respectively.

Goethite recrystallization: Goethite (G) was synthesized from hydrothermal alteration of poorly crystalline ferrihydrite (FH) precursors described above, following a modified procedure from Schwertman (2000). [38] The ferrihydrite slurries (FH-C-3000, FH-C-1000, FH-C-400, FH-S-3000, FH-S-1000, FH-S-400) were adjusted to a pH of 10-11 using 1-5 mol/L KOH. The samples were placed in capped 30 mL Savillex® PFA vials under atmospheric conditions and aged at 80º C for 72 hours in an oil bath to induce ferrihydrite recrystallization to goethite. The goethite samples will be referred to as G-FH_C-3000, G-FH_C-1000, G-FH_C-400, G-FH_S-3000, G-FH_S-1000, and G-FH_S-400.

After ferrihydrite and goethite synthesis, the supernatant was analyzed for Pu content via LSC. In preparation for the various microscopy and spectroscopy performed on the solid phase, the solids were rinsed and centrifuged (4000 RCF, 5 minutes) three times in Milli-Q water to remove soluble salts (18.2 MΩ·cm). After each rinse the supernatant was analyzed for Pu via LSC.

Powder x-ray diffraction

All Pu doped goethite samples were prepared for powder x-ray diffraction (P-XRD) using a Bruker-D8 diffractometer from (5-70º 2θ). 8-10 mg samples were loaded on a domed zero background slide. The domed sample holder is necessary to avoid dispersion of radioactive materials; however, it introduces a high background especially at low angles. The introduction of high background at low angles makes it difficult to identify the presence of poorly crystalline-amorphous material in the samples. For ferrihydrite, a Pu-free sample (FH-blank) was prepared following the methodology described above, so that x-ray diffraction measurements could be performed without the use of a domed sample holder.

174 ***Oxalate extraction***

175 To quantify ferrihydrite recrystallization to goethite, an oxalate extraction method was used. [38]
176 For the oxalate extraction, 1 mL of a pH 3 0.2 mol/L ammonium oxalate and 0.2 mol/L oxalic acid
177 solution was added to a 2 mL (1 g/L) mineral slurry aliquot. The samples (G-FH_S-3000, G-FH_S-
178 1000, G-FH_C-3000, and G-FH_C-1000) were then reacted in the absence of light on a shaker table
179 for 2 hours to dissolve any non-crystalline component. After 2 hours the samples were centrifuged
180 (5 minutes, 4000 RFC) and the Fe concentration in the supernatant was determined via inductively
181 coupled plasma mass spectrometry (Thermo Fisher Scientific ICAP-Q quadrupole ICP-MS). The
182 oxalate extraction was also performed on one of ferrihydrite sample (FH-S-3000).

183 ***Transmission electron microscopy***

184 Mineral samples were suspended in ethanol (ferrihydrite) or Milli-Q water (18.2 MΩ·cm)
185 (goethite), sonicated for 5 minutes and added drop-wise onto a copper-supported lacy carbon grid.
186 The samples were imaged using a Titan (FEI) microscope. Imaging was conducted at 300 kV using
187 scanning electron and z-contrast modes. Energy dispersive spectroscopy analyses were performed
188 for selected areas and spots using a FEI SuperX G2 with quad silicon drift detectors. The structure
189 of Pu colloids was investigated using high-resolution transmission electron microscopy (HR-
190 TEM) and scanning transmission electron microscopy (STEM).

191 ***Pu acid extraction***

192 Sequential acid extraction was performed to determine the leachability of Pu from the Pu doped
193 goethite samples (G-FH_S-3000, G-FH_S-1000, G-FH_C-3000, and G-FH_C-1000). Mineral
194 suspensions (0.33 g / 100 mL) were equilibrated in increasingly higher molarity HNO_3 solutions
195 (0.001-4 M) for 30 minutes. After 30 minutes extractions, the mineral-acid suspensions were
196 centrifuged (10 minutes, 8500 RCF) and the supernatant was analyzed to determine the Pu

197 concentration via LSC. For both G-FH_C-3000 and G-FH_S-3000 the mineral suspensions in 4 M
198 HNO_3 were reacted for an additional 24 hours. Samples were then centrifuged (10 minutes, 8500
199 RCF) and the Pu concentrations in the supernatant were measured. A parallel experiment was
200 performed on Pu-free goethite to determine the leachability of Fe. Fe concentrations in leached
201 solutions were determined via ICP-MS (Thermo Fisher Scientific ICAP-Q quadrupole ICP-MS).

202 ***Extended x-ray absorption fine structure spectroscopy***

203 Selected ferrihydrite and goethite mineral phases were isolated from the experiments via
204 centrifugation (5 minutes, 4000 RCF), mixed with glycerol, and mounted into custom made indium
205 sealed, triple contained, aluminum sample holders. All EXAFS data were collected on beamline
206 11-2 at the Stanford Synchrotron Radiation Lightsource, Stanford CA. Pu L_{III}-edge (18057 eV)
207 EXAFS data were collected in fluorescence mode using a 100 element Canberra Ge detector
208 (corrected for dead time) with a Si(220) (ϕ=0°) double monochromator detuned to 50% intensity.
209 All samples were held in a LHe cryostat at 30 K throughout analysis. Data reduction and analysis
210 were conducted using the RSXAP software suite [59, 60, 61] in conjunction with backscattering
211 lineshapes and phases calculated using FEFF8.5L. [62] The EXAFS data were transformed between
212 2.5 and a maximum of 12 $Å^{-1}$ using a Gaussian window with a width of 0.3 $Å^{-1}$ and all fitting was
213 conducted in R-space. Error analysis was performed using a profiling method. [63] In all cases to the
214 total number of fitting parameters was less than two-third of the total number of independent
215 points.

216 **Results and discussion**

217 This study focused on understanding the environmental behavior of Pu in the presence of iron
218 oxy(hydroxides), ubiquitous minerals that commonly form in aqueous environments and/or
219 secondary minerals resulting from steel corrosion. Specifically, we investigated Pu behavior

during the formation of ferrihydrite and its subsequent transformation to goethite. Ferrihydrite was synthesized with various amounts of Pu(IV) following either a sorption or coprecipitation process, prior to goethite crystallization. We then used a series of characterization techniques to interrogate the nature of Pu associated with the iron (oxy)hydroxides.

Ferrihydrite and goethite synthesis in the presence of Pu(IV). After ferrihydrite and goethite were synthesized, the minerals were characterized by P-XRD, TEM, and oxalate extraction. P-XRD of all goethite samples (G-FH_S-3000, G-FH_S-1000, G-FH_S-400, G-FH_C-3000, G-FH_C-1000, G-FH_C-400) were collected, and additional peaks beyond those characteristics of goethite were not identified (Figure 1). The P-XRD pattern of ferrihydrite was collected for FH-blank, a Pu free sample, and the broad peaks at 34° and 65º of 2θ are characteristic of two-line ferrihydrite. [38] TEM photomicrographs of the solid samples illustrate the crystal morphology of nanocrystalline FH-C-3000, G-FH_S-3000, and G-FH_C-3000 (Figure SI 1). The ferrihydrite nanoparticles are poorly crystalline and range in size between 3-5 nm, whereas the acicular goethite grains are crystalline and are 100s nm long and 10s nm wide. These crystal morphologies are consistent with ferrihydrite and goethite materials. [38] Oxalate extraction of, G-FH_S-3000, G-FH_S-1000, G-FH_C-3000, and G-FH_C-1000 confirmed that > 99 % of ferrihydrite recrystallized to more ordered forms. As expected, the oxalate extraction of FH-S-3000 showed a total recovery of Fe (99.99%). The P-XRD, TEM analysis and oxalate extraction results indicate that the addition of Pu does not affect the nature of the synthesized products (Figure 1).

The analysis of the supernatant from all ferrihydrite syntheses indicated that 99.9% of Pu had been removed from solution upon reaching the desired pH of ~8. After ferrihydrite hydrothermal aging to goethite, the concentration of Pu in the supernatant was monitored again. The percentage of Pu remaining in the supernatant was $< 0.2 \pm 0.08$ % for G-FH_S-1000, G-FH_S-3000, G-FH_C-1000, and

G-FH_C-3000, whereas for G-FH_S-400 and G-FH_C-400 it ranged between 0.6-0.8%. The results indicate that a strong association between Pu and the iron (oxy)hydroxide solids is preserved during the recrystallization process.

The HR-TEM imaging and elemental mapping of G-FH_S-3000, G-FH_S-1000 revealed the presence Pu nanoparticles on the mineral samples. As calculated from several TEM images, the size of the nanoparticles ranges from 3 to 5 nm, which is consistent with the 2.5-5 nm size range for PuO_2 reported in the literature. [14, 50] Electron diffraction, HR-TEM analysis confirm that the observed nanoparticles have the expected *fcc* PuO_2 structure with Fm3m space group (d1 (Å) 3.08(0.01) and d2 (Å) 2.61(0.02)) [14] (Figure 2). The observed PuO_2 structure is in contrast to the Pu_4O_7 nanoparticles structure observed on goethite observed by Powell et al (2011)[52]; although, it should be noted that the experiments were not the same. This suggests that the sorption of Pu to goethite surfaces during recrystallization from ferrihydrite may not be the result of epitaxial growth of Pu nanoparticles. Rather, the presence of PuO_2 nanoparticles on goethite may be due to their formation during the initial ferrihydrite precipitation and preservation during the recrystallization process. Nevertheless, the presence of Pu nanoparticulate in these samples is not unexpected: starting at circumneutral pH values, Pu(IV) is generally expected to undergo rapid hydrolysis to form PuO_2 solids.

HR-TEM imaging revealed the presence of PuO_2 precipitates (*fcc*, d1 (Å) 3.08(0.02) and d2 (Å) 2.61(0.02)) in the high Pu concentration G-FH_C-3000 (

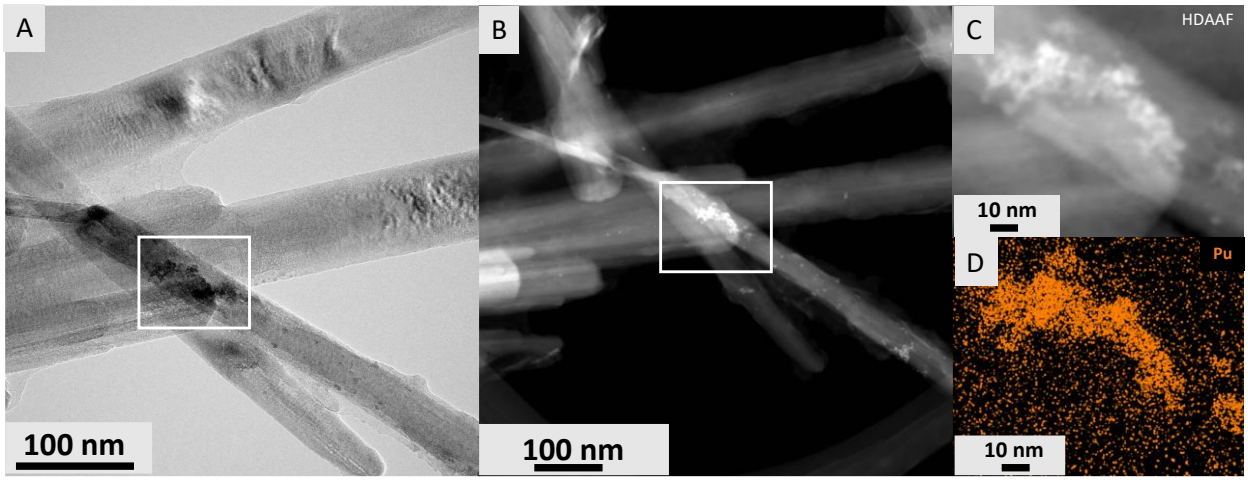

Figure 3); however PuO_2 nanoparticles were not identified in G-FH_C-1000 and G-FH_C-400. Furthermore in G-FH_C-1000 and G-FH_C-400 the Pu concentration was too low to be detected using STEM-TEM indicating that Pu is either dispersed on the surface of goethite and/or incorporated into the solid phase. The TEM imaging of the precursor FH-S-3000 and FH-C-3000 samples was inconclusive. Unfortunately, the ferrihydrite nanoparticles are 3-5 nm in size, which is similar to the PuO_2 nanoparticles size characterized in this study. This similarity in size between Pu nanoparticles and the ferrihydrite substrate creates difficulties in the identification and distinction of PuO_2 via TEM imaging. For this reason Pu nanoparticles could not be identified via TEM analysis of the ferrihydrite samples (FH-S-3000 and FH-C-3000).

Reversibility of Pu associated with ferrihydrite and goethite. In an effort to understand the reversibility of the Pu associated with the goethite, sequential acid leaching experiments were performed. Differences in the amount of Pu desorbed from the mineral surfaces were observed between goethite samples recrystallized from both the sorption and coprecipitation process of ferrihydrite. A total of 9.6 ± 0.2% and 3.42 ± 0.3% are leached from G-FH_S-3000 and G-FH_S-

277 1000, respectively, whereas in comparison 4.03(12)% and 1.54(8)% of Pu are leached in solution
278 from G-FH$_C$-3000 and G-FH$_C$-1000, respectively. After 24 hours of leaching in 4 mol/L HNO_3, a
279 total of 40(1)% of Pu is leached from G-FH$_S$-3000; whereas only 7.5(5)% of total Pu is leached
280 from G-FH$_C$-3000. In the Pu-free goethite leaching test, < 0.05 ± 0.003 % Fe was dissolved after
281 24 hours, indicating that the goethite does not go through extensive dissolution in the tested
282 experimental conditions (Figure SI 1).
283 The acid leaching results show that overall more Pu is leached from goethite hydrothermally
284 aged from ferrihydrite synthesized following the sorption than the coprecipitation method. Such
285 experiments could not be performed on the ferrihydrite samples due to the enhanced dissolution
286 of ferrihydrite in the chosen experimental conditions, nonetheless differences in the amount of Pu
287 leached were observed between goethite samples recrystallized from the sorption or
288 coprecipitation process of ferrihydrite. Overall, in ~ 4 hours (

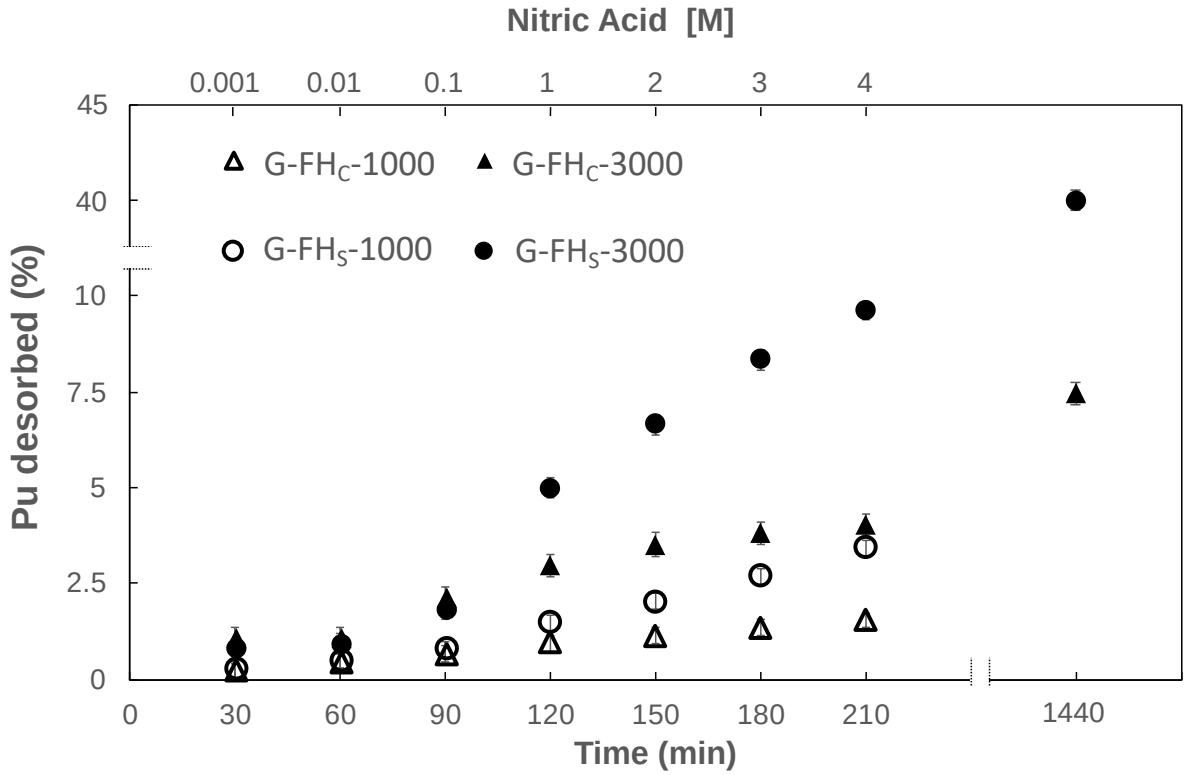

289

Figure 4), 2-3 times more Pu is leached from goethite recrystallized following the sorption process, compared to the coprecipitated samples. Differences in synthetic pathways may have an impact on the nature of Pu association with the mineral in both the ferrihydrite precursor and in the hydrothermally aged product (goethite). These results also suggest that Pu sorbed to ferrihydrite may be more labile that Pu coprecipitated into ferrihydrite, even after recrystallization to goethite. This, in turn, suggests that some properties of Pu association with the precursor mineral are retained through recrystallization process.

The structure of Pu associate with ferrihydrite and goethite using EXAFS

A representative set of ferrihydrite and goethite samples were analyzed using EXAFS spectroscopy in order to develop a mechanistic understanding of the the nature of the Pu binding with these mineral phases. Three samples following the sorption method, FH-S-3000, G-FH_S-3000, and G-FH_S-1000 were analyzed in addition to four samples that were produced from the coprecipitated method, FH-C-3000, G-FH_C-3000, G-FH_C-1000, and G-FH_C-400. The background-subtracted Pu L_{III}-edge EXAFS spectra and the corresponding Fourier transforms (FT) for ferrihydrite and goethite systems are shown in Figure 5 and Figure 6, and fitting results for all datasets are detailed in Table 1**Erreur ! Source du renvoi introuvable.**.

Ferrihydrite

For FH-S-3000 the dataset was successfully modeled with a single Pu-O shell consisting of 9(1) scatterers (i.e. coordination number) at 2.31(1) Å. A further two peaks were evident in the FT at r > 2.5 Å. Note that we refer to the x-axis of the FT as r, and pair distances as R. The first of the two peaks was successfully modeled as 6(2) Pu-Fe scatterers at 3.39(1) Å with an elevated Debye Waller factor (σ^2; pair-distance distribution variance) of 0.021(4) $Å^2$, which implies a broad distribution of Pu-Fe distances. The second peak was modeled with 3(1) Pu-Pu scatterers at 3.79(1)

313 Å, consistent with expectations for PuO_2 (3.82). [64] Given the identification of both Pu and Fe
314 scatterers in the EXAFS it is very likely that in FH-S-3000 Pu(IV) is present in two distinct
315 coordination environments: PuO_2, and an additional adsorbed, poorly defined, inner-sphere
316 complex on the ferrihydrite surface. Recent reports of various actinides (Th, U and Pu and Np)
317 adsorbed onto Fe containing minerals show An-Fe distances varying from 3.35-3.7 Å [43, 65-69],
318 consistent with our modeled 3.39(1) Å Pu-Fe distance. It is difficult to quantify the relative
319 proportions of these two Pu species (inner-sphere and PuO_2) as EXAFS analysis only provides an
320 average coordination environment around the Pu atom. However, we can use our knowledge of
321 the PuO_2 structure to try and bracket the relative proportions of the two phases. The structure of
322 bulk PuO_2 consists of 12 Pu atoms at 3.82 Å.[64, 66] The number of Pu atoms reduces as PuO_2 moves
323 away from a bulk material into a nanoparticulate form due to Pu atoms near the surface having
324 fewer Pu neighbors, thereby reducing the average coordination number in a particle. [66, 70] If we
325 assume that the PuO_2 nanoparticles are on average 4 nm, as the TEM analysis of G-FH_S-3000 and
326 G-FH_S-1000 indicates, this would correspond to an average of 10 Pu-Pu scatterers (Figure SI 3).
327 [71] Using this assumption we can estimate that approximately 30% of all Pu in FH-S-3000 is present
328 as PuO_2 with the remainder existing as an inner sphere complex with the ferrihydrite. The inherent
329 uncertainty of estimating an average particle sizes using TEM and coordination numbers using
330 EXAFS mean that this calculation of the proportion of nanoparticulate vs surface adsorbed Pu is
331 at best a rough approximation. We can constrain this value further by assuming that all PuO_2 has
332 12 Pu-Pu scatterers, which would suggest the minimum proportion of PuO_2 in this sample is ~25%.
333 However, if the average PuO_2 particle size (and therefore the number of Pu-Pu scatterers) is less
334 then suggested by TEM analysis the true proportion of PuO_2 could be much greater than our
335 calculations suggest.

The EXAFS spectrum of Pu associated with FH-C-3000 was successfully modeled with a split O environment, including 3.0(1) and 4.0(2) Pu-O scatterers at 2.24(1) and 2.41(1) Å. In contrast to the FH-S-3000 dataset, one additional peak was evident in the FT which was successfully fit with a single Pu-Fe shell at 3.39(1) Å. Interestingly this shell was fit with a high number (8 ± 1) of Pu-Fe scatterers albeit with a very high σ^2 of 0.026(3) $Å^2$. The high uncertainties associated with this fit make the exact nature of the Pu-ferrihydrite complex difficult to elucidate, but it could represent a replacement of the Fe^{3+} ion with a Pu^{4+} in the ferrihydrite solid. The large discrepancy in the size of Fe^{3+} and Pu^{4+} ions (0.645 and 0.96, respectively [72]) make this substitution unlikely without significant disruption to the local structure. However, our EXAFS data do indicate highly elevated σ^2 suggesting a broad range of Pu-Fe pair distances, and lack long-range order that would be evidenced by multiple Pu-Fe shells. The local environment around Fe in the ferrihydrite structure consists of Fe atoms at ~3.04 and 3.44 Å, although due to the poorly crystalline nature of ferrihydrite, its structure has still not been fully resolved. [35, 73] Although highly disordered a Pu-Fe distance of 3.39(1) Å could correspond to corner sharing between metal polyhedral in the ferrihydrite structure. [73, 74]

The σ^2 and coordination number parameters in the EXAFS equation are commonly correlated in the fit results; [75] therefore, the elevated σ^2 fitted here suggests either a large amount of structural disorder (i.e. a broad distribution of Pu-Fe pair distances) or that the number of Pu-Fe scatterers is being overestimated. For example, constraining the number of Pu-Fe scatterers to 4 reduced σ^2 to 0.013(2) $Å^2$ while still maintaining a reasonable fit albeit with an increased correlation factor (*R* %) (7.9 vs 3.5 %); thus, it cannot be excluded that the EXAFS data may represent a surface complex with a lower number of Pu-Fe scatterers. [43, 65-69] Interestingly, the EXAFS spectrum and resultant fit for FH-C-3000 bears a striking resemblance to what was collected in similar

experiments by Smith et al., [43] where ferrihydrite precipitation was induced from a Pu-HNO_3 solution at pH 9. PuO_2 formation was not observed and the data were modeled with 4 Fe scatterers at 3.38(2) Å and attributed it to the formation of a polynuclear multidentate complex with the ferrihydrite surface. In contrast to the FH-S-3000 dataset no Pu-Pu scatterers could be identified in the FH-C-3000 EXAFS precluding the possibility of PuO_2 formation in this sample and demonstrating that Pu(IV) is associated with the ferrihydrite solid before PuO_2 precipitation could occur.

Goethite

The EXAFS spectra of the goethite samples recrystallized from the hydrothermally altered Pu-sorbed ferrihydrite (G-FH_S-3000 and G-FH_S-1000) are similar and both datasets could be fit using a two-shell model. The first shell in both cases was successfully fit with 8(1) Pu-O scatterers at 2.32(1) Å and the second peak in the FT was fit with 4(1) Pu-Pu scatterers at 3.80(1) Å strongly supporting the formation of PuO_2 solids in these systems. However, the modeled Pu coordination numbers are low compared to expectations for PuO_2 and suggest either PuO_2 is present as very small nanoparticulate < 1 nm (Figure S2) or that a second Pu species is present as an adsorbed or coprecipitated inner sphere complex. We can use a similar approach with this dataset as we used with the FH-S-3000 dataset and attempt to put some limits on the quantity of PuO_2 present. With the number of Pu-Pu scatterers in both samples being fitted as 4(1) and the expectation of bulk PuO_2 being 12 the minimum amount of PuO_2 present in this system would be 33%. In this case, if the TEM characterized particles are representative of the average, the remaining Pu would have to be present as a surface complex. Unfortunately, while it was possible to include Pu-Fe scatterers in the fit they were unable to pass an F-test so we cannot conclusively demonstrate an inner-sphere surface complex, however, this does not exclude the possibility of a surface complex entirely. For

example, Pu may be present as weakly bound outer-sphere complex or as an inner sphere complex with a very broad range of Pu-Fe pair distances making it very difficult to discern using EXAFS analysis.

Overall the EXAFS fits and TEM characterization support PuO_2 formation in G-FH_S-3000, G-FH_S-1000. The EXAFS data also suggest that Pu in these samples may be present in dual coordination environment with PuO_2 accounting for a minimum of 33% of Pu, and Pu not associated with PuO_2 being present as poorly defined surface complex since no Pu-Fe scatterers could be conclusively identified in this sample. [11, 12] The high percentage of Pu detected in the acid extraction of G-FH_S-3000 and G-FH_S-1000, is consistent with the presence of Pu as a Pu surface complex, where the leached fraction could represent any weakly bound Pu being easily leached from the goethite surface. Collectively, these data demonstrate that in the ferrihydrite and goethite samples synthesized following the sorption method a large fraction of Pu will be found as intrinsic PuO_2 nanoparticles, and the PuO_2-like coordination environment is preserved during mineral recrystallization. The EXAFS data also demonstrates that Pu adsorbed to ferrihydrite may be remobilized, as evidenced by the changes in coordination environment of the Pu sorbed species from the ferrihydrite precursor (FH-S-3000) to the recrystallized products (G-FH_S-1000 and G-FH_S-3000).

The EXAFS spectrum of the Pu associated with G-FH_C-3000 was successfully modeled with 6(1) Pu-O scatterers at 2.28(1) Å and 1 (1) Pu-Fe scatterers at 3.56(1) with σ^2 values of 0.013(2) and 0.003(1) $Å^2$, respectively. Additionally, a peak at 3.7 Å was successfully modeled as 2(1) Pu-Pu scatterers at 3.80(1). The clear identification of a Pu-Pu scatterers in the FT demonstrates the presence of PuO_2, and is consistent with the identification of PuO_2 nanoparticles imaged via TEM. Interestingly, no PuO_2 was observed in the ferrihydrite precursor (FH-C-3000) for this sample

indicating that Pu(IV) was probably excluded from the ferrihydrite structure or surface in the recrystallization reaction where it subsequently underwent precipitation as PuO_2. As with the other observations of Pu-Pu scatterers in other samples presented here, the low coordination numbers suggest PuO_2 accounts for only a fraction of all Pu in this sample. A pair of Pu-Pu scatters would imply a minimum of 17% PuO_2 in this experiment, however, due to the nanoparticulate nature of the PuO_2 this could be far higher. The presence of Pu-Fe peaks suggests that the non-PuO_2 fraction of Pu in this sample may be present as an inner sphere complex adsorbed on the surface of goethite.

The G-FH_C-1000 and G-FH_C-400 samples displayed similar spectra with three easily identifiable peaks in the FT at r ≈1.5 Å, 2.5 Å, and 3.2 Å. The first peak at 1.5 Å were successfully fit with an Pu-O shell 6(1) scatterers at 2.21(1) Å. Oxygen shells in both G-FH_C-1000 and G-FH_C-400 had σ^2 factors of 0.013(2) and 0.016(2) $Å^2$ implying a broad distribution of Pu-O pair distances. This reduction in O coordination from 8 in the other systems to 6 here is interesting as the Fe^{3+} is coordinated by 6 oxygen atoms in the goethite structure. The second and third features in the FT were too short to be associated with Pu-Pu scatterers therefore they were modeled as two Fe shells. These were fitted as 6(1) Pu-Fe scatterers at 3.17(4) Å and 10(8) Pu-Fe scatterers at 3.49(2) Å with an elevated σ^2 factor of 0.010(1) $Å^2$ for the G-FH_C-1000 dataset. This result was similar to the G-FH_C-400 dataset where the second and third features in the FT were fit as 5(3) Pu-Fe scatterers at 3.19(1) Å and 8(4) Pu-Fe scatterers at 3.47(2) Å. The high number of Fe atoms and the large estimated errors associated with those parameters in G-FH_C-1000 and G-FH_C-400 makes it difficult to draw any firm conclusions about the exact nature of the local structure in the Pu-goethite complex; however, the data could indicate some kind of incorporation into the goethite structure. The local environment around Fe in the goethite structure consists of 2, 2, and 4 Fe neighbors at ~3, ~3.3 and ~3.4 Å, respectively. [76, 77] These distances are not unlike our fitted

distances of 3.2 and 3.5 Å and, given the large error bars associated with our fits our data is compatible with Pu^{4+} incorporated into goethite. As was discussed previously the difference in size between Fe^{3+} and Pu^{4+} make direct and stable substitution into the goethite structure unlikely without significant disorder in the local and long-range structure. Interestingly, the σ^2 in our fits do suggest elevated levels of local structural disorder around the Pu atom. Other possible explanations for the local Pu structure observed are the formation of a surface complex on the goethite surface; however, the shortest modeled Pu-Fe distance at 3.19(2) Å is significantly shorter than the range of An-Fe distances previously reported (3.35-3.7 Å). [43, 65-69] Lastly the EXAFS data are not inconsistent with the formation of a distinct poorly ordered Pu-Fe solid phase as has been hinted at in forensics literature, [56] although the formation of a distinct Pu-Fe phase was not supported by TEM imaging. Overall the TEM and EXAFS data demonstrate that PuO_2 exists at the highest concentration Pu coprecipitation samples (3000 ppm) but not the lower concentrations (1000 and 400 ppm). This suggests that during ferrihydrite recrystallization at higher Pu concentration (0.06 mmol/L Pu(IV) in solution, 3000 ppm Pu(IV) in the solid) part of the Pu associated to the ferrihydrite precursor FH-C-3000 will be remobilized and will form PuO_2 nanoparticles. Furthermore there is evidence that during the recrystallization process at high Pu concentration a fraction of the Pu remains strongly bound to the goethite surface (Table 1). No PuO_2 was observed in the ferrihydrite precursor (FH-C-3000) and in the lower concentration goethite samples (G-FH_C-1000 and G-FH_C-400). The presence of two distinct Pu-Fe shells in G-FH_C-1000 and G-FH_C-400 (at 3.20 Å and 3.49 Å) compared to the ferrihydrite precursor FH-C-3000 (one shell at 3.41 Å) suggest that the Pu binding site changes significantly during iron oxide recrystallization. Even though Pu coordination changes during recrystallization, these experimental conditions do not favor PuO_2 precipitation. It is difficult to determine the exact nature

of Pu in solids prepared following the coprecipitation process; however, the data clearly show that Pu is strongly bound to the minerals either by the formation of a strong inner sphere complex, or via an incorporation process.

Conclusions

In this study we investigated the fate of Pu during iron oxide recrystallization processes via TEM imaging, EXAFS and chemical analysis. We show that variations in synthetic routes have impacts on the nature of Pu associated with both the ferrihydrite precursor and the ferrihydrite recrystallization product (goethite). When a Pu containing solution is added to a ferrihydrite mineral (sorption route), a fraction of the Pu precipitates as PuO_2 nanoparticles and the remaining Pu fraction forms a complex on the mineral surface. After hydrothermal alteration to goethite, the PuO_2-like nanoparticle is preserved, and a fraction of Pu is still present as a surface adsorbed species on the goethite mineral surface. There is evidence that this adsorbed species is more weakly bound to goethite than to ferrihydrite, as evidenced by a decrease in the number of Pu-Fe scatterers identified in the respective sample. This observation suggests that Pu adsorbed to ferrihydrite may be mobilized during the recrystallization processes. The analysis of the supernatant after hydrothermal alteration of ferrihydrite to goethite showed a small increase in Pu concentration confirming that some Pu re-mobilization occurs during mineral recrystallization processes.

When ferrihydrite is precipitated directly from a solution containing Fe and Pu (coprecipitation route) no PuO_2 is observed. Although it is difficult to identify the exact nature of Pu in the sample due to a high degree of disorder, there is evidence that Pu is strongly bound to the ferrihydrite solids through a combination of adsorption and/or coprecipitation as evidenced by the high number of Pu-Fe scatterers. In this sample a fraction of Pu could coprecipitate with ferrihydrite and/or form a polynuclear inner sphere complex. The EXAFS data show that the Pu binding site changes significantly during ferrihydrite recrystallization, indicating that Pu is mobilized during

475 hydrothermal alteration; however, only a small fraction of Pu in the highest Pu concentration
476 samples (G-FH_C-3000) is remobilized to form PuO_2. In all goethite samples Pu is strongly sorbed
477 (either coprecipitated and/or adsorbed as inner sphere complex) to the goethite as evidenced by
478 the high number of Pu-Fe scatterers. The acid leaching results support this conclusion by showing
479 that less Pu is accessible to leaching in goethite formed via coprecipitation process, compared to
480 the goethite formed via the sorption process. These observations confirm that that the nature of Pu
481 associated with the mineral will affects the leachability of Pu from the solids.
482
483 **Implications for the natural and engineered environment**

484 Our results showed that variations in the synthetic routes (sorption vs. coprecipitation) of
485 ferrihydrite at pH ~8 impact the nature of Pu associated with the mineral. The major difference
486 between the two synthetic processes is the timing of Pu addition to the ferrihydrite precipitate and
487 we expect both processes to be of environmental relevance. For example, the sorption method,
488 where Pu is added at pH ~8 to an already formed ferrihydrite, simulates a simple scenario where
489 Pu becomes associated with a preexisting mineral substrate. In the coprecipitation method a Pu-
490 ferrihydrite precipitate is formed from neutralizing the pH of an acidic solution containing
491 dissolved Pu and Fe. This synthetic method likely simulates a scenario where an acidic plume is
492 neutralized for remediation purposes or where changes in geochemical conditions occur in a
493 contaminated streams or ponds. Secondary iron (oxy)hydroxides with associated Pu and other
494 radionuclides have been identified in surface contaminated waters in a pH range of 5.9-8.2 [55, 57, 79]
495 and although the mechanisms of formation of these radioactive particles is still unclear, both
496 sorption and secondary mineral formation processes are likely involved . [55, 57, 79]

Our results also show that differences that exist in the Pu association with the precursor material are retained through the recrystallization to goethite. The hydrothermal alteration to goethite however was conducted in the alkaline to hyperalkaline pH range (~10-11). Many underground repository concepts utilize cementitious materials in the design as part of the engineered barrier system or as structural materials. [80] The pH during leaching of these materials upon resaturation will buffer to hyperalkaline conditions (pH 10.5−13.1), creating a plume of alkaline fluid in the host rock and/or local environment. [80] Furthermore, hyperalkaline conditions can prevail in many contaminated land scenarios, e.g., where cementitious building materials contact subsurface sediments [81, 82] and at the underground waste storage tanks at the Hanford Site in Washington State, USA.[83]

Overall the results presented in this study provide valuable new insights into Pu(IV)- iron (oxy)hydroxide interactions in the natural and engineered environment and highlight the importance of understanding the fate of radionuclides during mineral recrystallization processes.

Acknowledgments

This work was performed with funding from supported by the Spent Fuel and Waste Science and Technology campaign of the Department of Energy's Nuclear Energy Program and Department of Energy, Office of Science, Biological and Environmental Research, Subsurface Biogeochemical Research program (SCW1053). Work was performed under the auspices of the U.S. Department of Energy by Lawrence Livermore National Laboratory under Contract DE-AC52-07NA27344. Work at Lawrence Berkeley National Laboratory was supported by the Director, Office of Science, Office of Basic Energy Sciences, Division of Chemical Sciences, Geosciences, and Biosciences Heavy Element Chemistry Program of the U.S. Department of

519 Energy (DOE) under Contract No. DE-AC02-05CH11231. EXAFS measurements were
520 performed at beamlines 11-2 at the Stanford Synchrotron Radiation Lightsource, which is
521 supported by the U.S. Department of Energy, Office of Science, Office of Basic Energy Sciences
522 under contract no. DE-AC02-76SF00515.

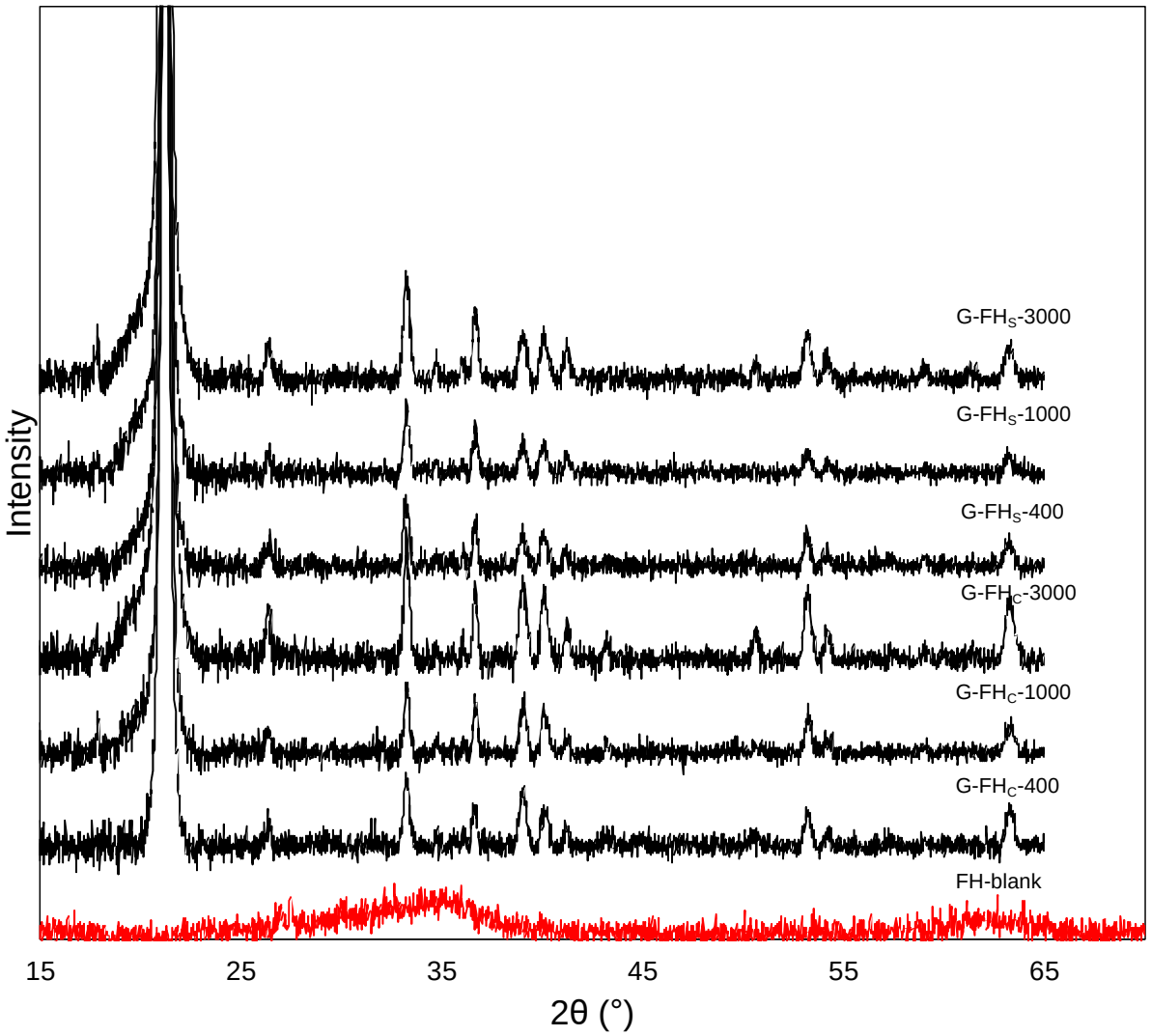

523

524 Figure 1: P-XRD pattern of Pu-free ferrihydrite (FH-blank), and goethite G-FH_C-3000, G-FH_C-
525 1000, G-FH_C-400, G-FH_S-3000, G-FH_S-1000 and G-FH_S-400.

526

527

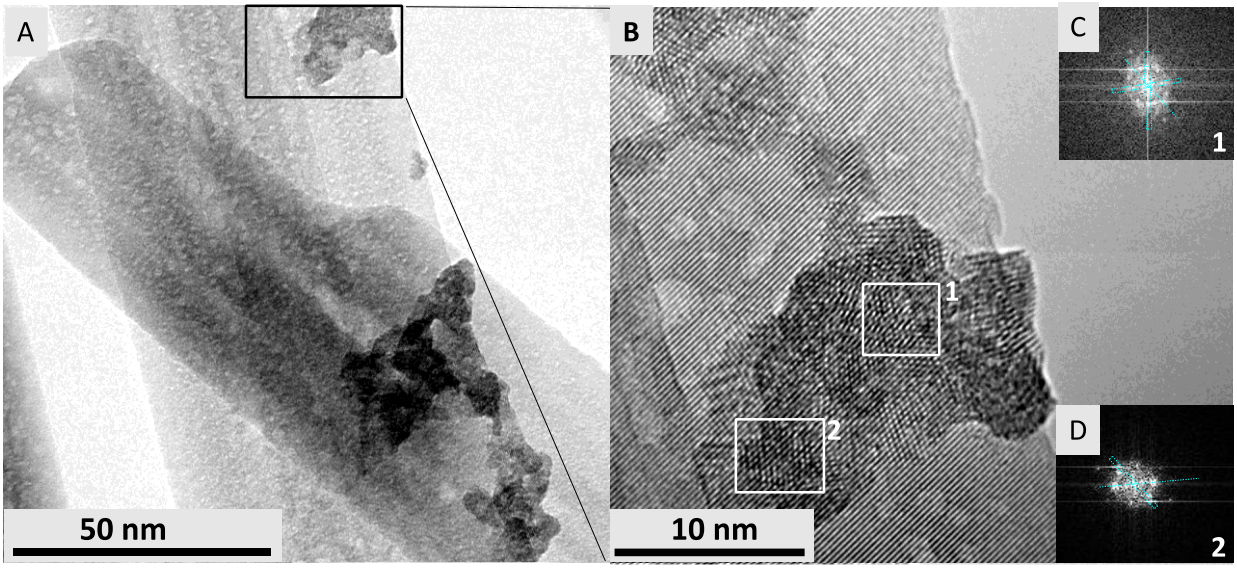

528

529 Figure 2: Pu nanoparticles on goethite G-FHs-3000. (A) Low-magnification TEM image of large
530 tabular goethite and intrinsic Pu nanoparticles (black inlet). (B) HRTEM image of Pu nanoparticles
531 on goethite surface from inlet in (A); (C) and (D) FFT of HRTEM area 1 and 2 shown in panel
532 (B), is consistent with the *fcc*, PuO_2 structure.

533

534

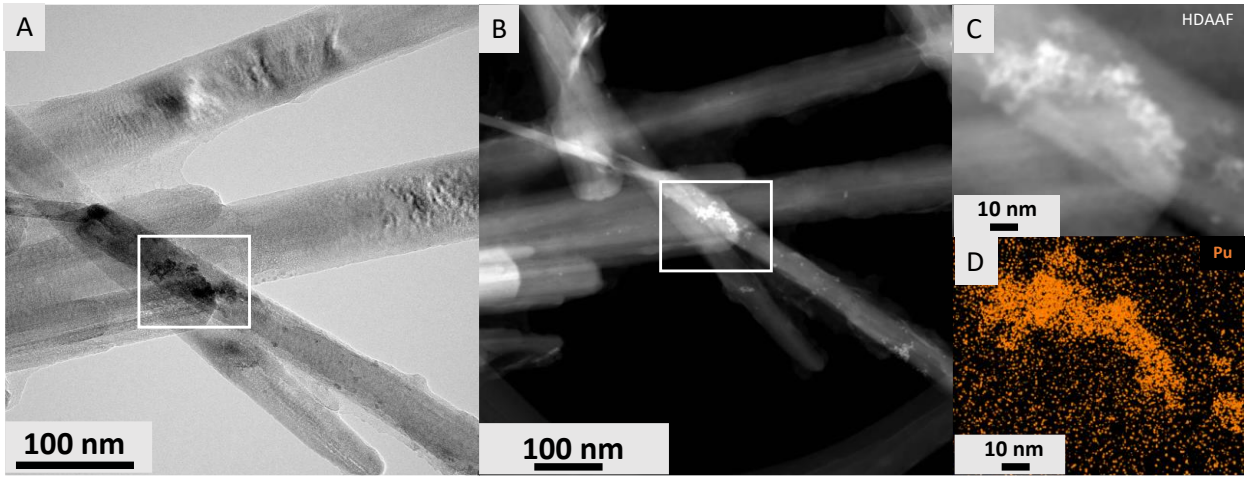

535

536 Figure 3: PuO_2 nanoparticles on goethite G-FH_C-3000. (A) Low-magnification TEM and (B)
537 STEM image of large tabular goethite and PuO_2 (white inlet). C) STEM and D) Pu elemental map
538 of Pu nanoparticles.

539

540

541

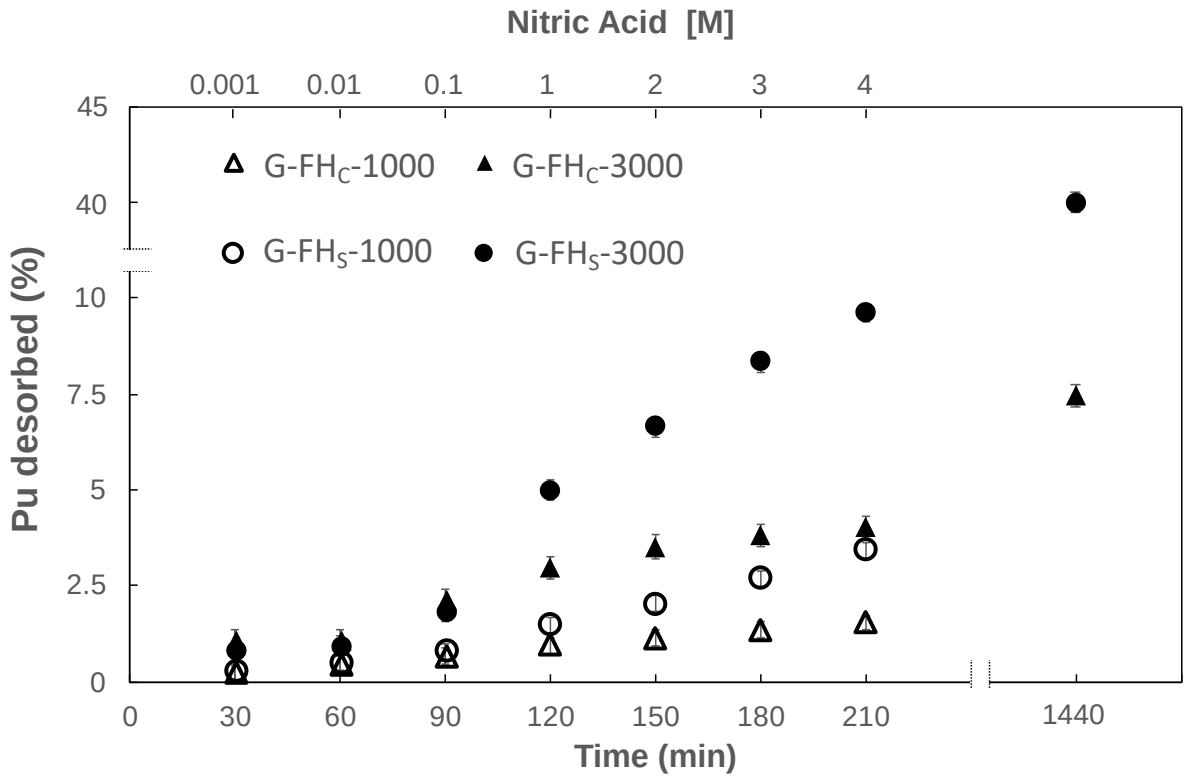

542

543 Figure 4: Leaching behavior of Pu in acidic solutions (0.001-4M) for goethite synthesized
544 following the sorption (G-FH$_S$-3000, G-FH$_S$-1000) and coprecipitation (G-FH$_C$-3000, G-FH$_C$-
545 1000) method.

546

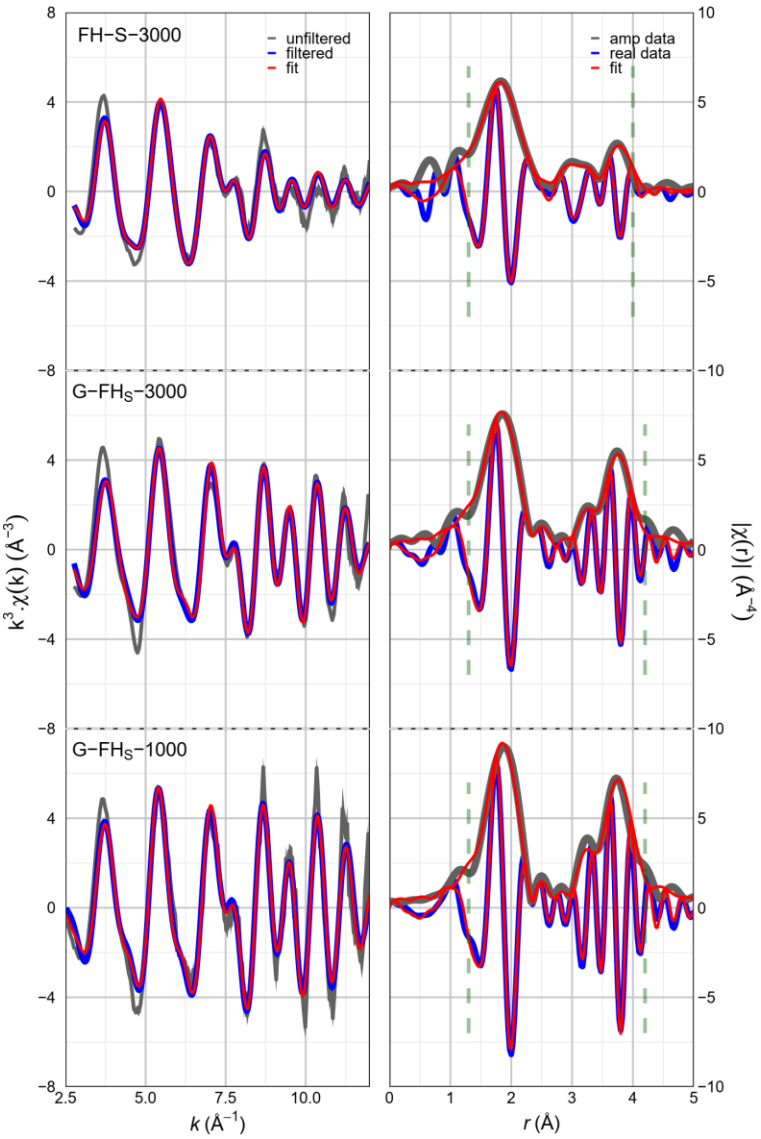

Figure 5: Pu L_{III}-edge EXAFS data and fit results for samples synthesized following the sorption method measured at 30 K. Left: Fourier transforms (FT) of the k-space data and fit. Vertical dashed lines indicate the fit range. Data were transformed between 2.5 and 12 $Å^{-1}$ by using a Gaussian window with a width of 0.3 $Å^{-1}$. The raw unfiltered data error bars (encompassed by the solid gray shaded area around the data set) were estimated by the standard deviation of the mean between traces. Right: EXAFS results in k-space.

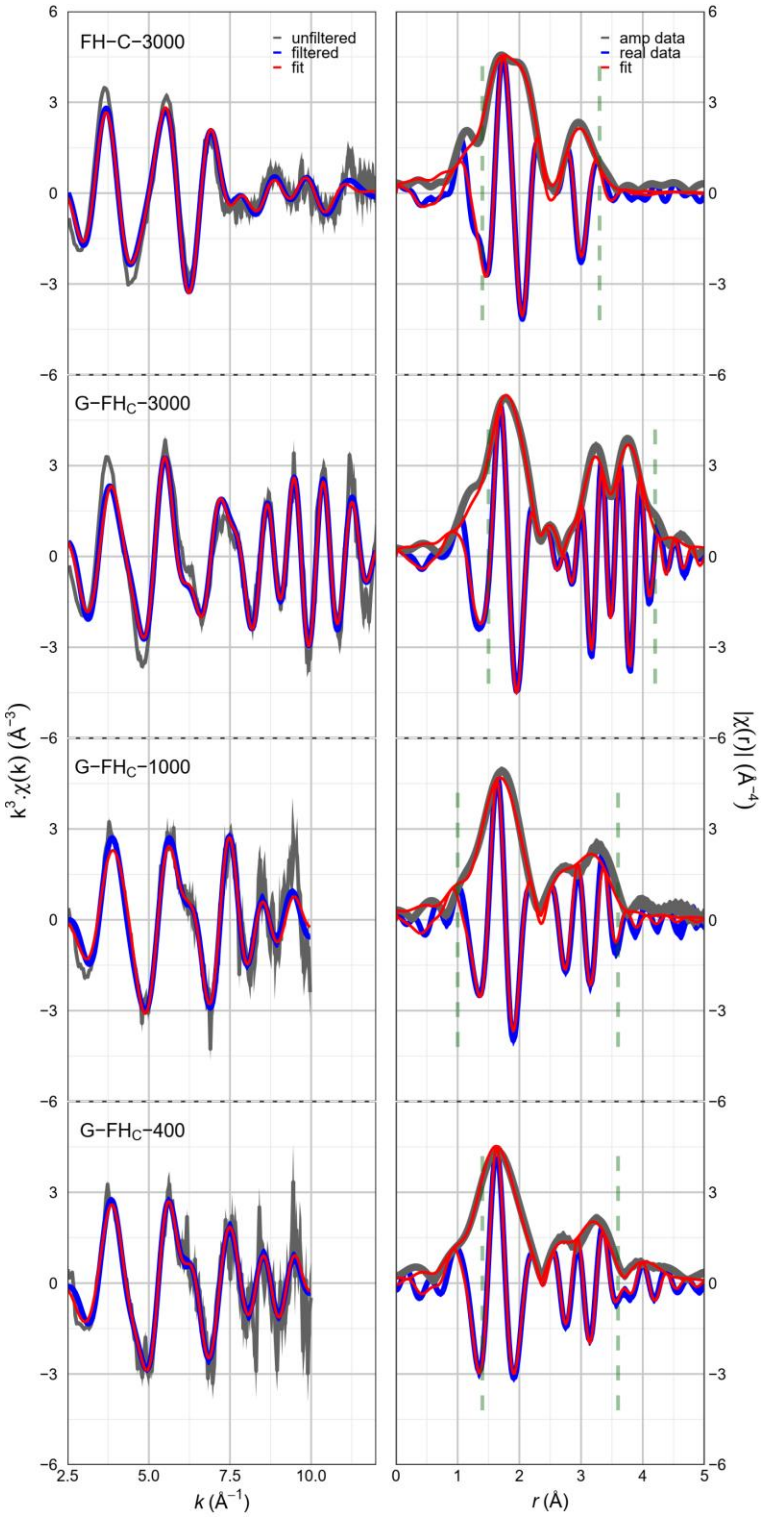

555

556 Figure 6: Pu L_{III}-edge EXAFS data and fit results for samples synthesized following the
557 coprecipitation method measured at 30 K. Left: Fourier transforms (FT) of the k-space data and

fit. Vertical dashed lines indicate the fit range. See Figure 5 for details. Right: EXAFS results in k-space.

Table 1: Summary of EXAFS fits

Sample	Shell	N	R (Å)	σ^2 (Å^2)	E0 (eV)	*R* (%)
FH-S-3000	Pu-O	9(1)	2.31(1)	0.014(1)	-10.8(8)	8.0
	Pu-Fe	6(2)	3.39(1)	0.021(4)		
	Pu-Pu	3(1)	3.79(1)	0.008(1)		
FH-C-3000	Pu-O1	4.0(2)	2.41(1)	0.005(1)*	-11.0(4)	3.5
	Pu-O2	3.0(1)	2.24(1)			
	Pu-Fe	8(1)	3.39(1)	0.023(2)		
G-FH$_S$-3000	Pu-O	8(1)	2.32(1)	0.010(1)	-11.4(8)	10.2
	Pu-Pu	4(1)	3.80(1)	0.003(1)		
G-FH$_S$-1000	Pu-O	8(1)	2.32(1)	0.008(1)	-11.7(7)	9.9
	Pu-Pu	4(1)	3.81(1)	0.001(1)		
G-FH$_C$-3000	Pu-O	6(1)	2.28(1)	0.013(2)	-12.6(12)	8.7
	Pu-Fe	1(1)	3.56(1)	0.003(4)		
	Pu-Pu	2(1)	3.80(1)	0.001(1)		
G-FH$_C$-1000	Pu-O	5(1)	2.21(1)	0.013(2)	-10.0(16)	13.3
	Pu-Fe	6(1)	3.17(4)	0.01(1)*		
	Pu-Fe	10(8)	3.49(2)			
G-FH$_C$-400	Pu-O	6(1)	2.20(2)	0.016(2)	-7.6(21)	12.2
	Pu-Fe	5(3)	3.19(2)	0.015(6)*		
	Pu-Fe	8(4)	3.47(2)			

*indicates a tied σ^2 parameter (i.e. shared in two shells). N represents the coordination number assuming an amplitude reduction factor of 1; R denotes the interatomic distance; σ^2 represents the Debye Waller factor; ΔE0 represents the energy shift from the calculated energy fermi level.

575

576 1. Choppin, G. R., Redox speciation of plutonium in natural waters. *Journal of*
577 *Radioanalytical and Nuclear Chemistry-Articles* **1991,** *147* (1), 109-116.
578 2. Sanchez, A. L.; Murray, J. W.; Sibley, T. H., The adsorption of plutonium IV and V on
579 goethite. *Geochimica et Cosmochimica Acta* **1985,** *49* (11), 2297-2307.
580 3. Begg, J. D.; Zavarin, M.; Edelman, C.; Kersting Annie , B., Sorption kinetics of
581 lutonium(V) to three montmorillonite clays. In *2018 Environemtal Suystem Science (ESS) PI*
582 *meeting*, Washington DC, 2018.
583 4. Efurd, D. W.; Runde, W.; Banar, J.; Janecky, D.; Kaszuba, J.; Palmer, P.; Roensch,
584 F.; Tait, C. D., Neptunium and Plutonium Solubilities in a Yucca Mountain Groundwater.
585 *Environmental science technology* **1998,** *32* (24), 3893-3900.
586 5. Neck, V.; Altmaier, M.; Seibert, A.; Yun, J. I.; Marquardt, C. M.; Fanghaenel, T.,
587 Solubility and redox reactions of Pu(IV) hydrous oxide: Evidence for the formation of
588 PuO2+x(s, hyd). *Radiochimica Acta* **2007,** *95* (4), 193-207.
589 6. Zhao, P. H.; Zavarin, M.; Leif, R. N.; Powell, B. A.; Singleton, M. J.; Lindvall, R. E.;
590 Kersting, A. B., Mobilization of actinides by dissolved organic compounds at the Nevada Test
591 Site. *Applied Geochemistry* **2011,** *26* (3), 308-318.
592 7. Icopini, G. A.; Lack, J. G.; Hersman, L. E.; Neu, M. P.; Boukhalfa, H.,
593 Plutonium(V/VI) Reduction by the Metal-Reducing Bacteria Geobacter metallireducens GS-15
594 and Shewanella oneidensis MR-1. *Applied and Environmental Microbiology* **2009,** *75* (11),
595 3641-3647.
596 8. Powell, B. A.; Fjeld, R. A.; Kaplan, D. I.; Coates, J. T.; Serkiz, S. M., $Pu(V)O_2^+$
597 adsorption and reduction by synthetic magnetite (Fe_3O_4). *Environmental Science & Technology*
598 **2004,** *38* (22), 6016-6024.
599 9. Zavarin, M.; Powell, B. A.; Bourbin, M.; Zhao, P.; Kersting, A. B., Np(V) and Pu(V)
600 Ion Exchange and Surface-Mediated Reduction Mechanisms on Montmorillonite. *Environ. Sci.*
601 *Technol.* **2012,** *46* (5), 2692-2698.
602 10. Begg, J. D.; Zavarin, M.; Kersting, A. B., Desorption of plutonium from
603 montmorillonite: An experimental and modeling study. *Geochimica Et Cosmochimica Acta*
604 **2017,** *197*, 278-293.
605 11. Choppin, G. R., SOLUTION CHEMISTRY OF THE ACTINIDES. *Radiochimica Acta*
606 **1983,** *32* (1-3), 43-53.
607 12. Clark, D. L.; Hobart, D. E.; Neu, M. P., Actinide Carbonate Complexes and their
608 Importance in Actinide Environmental Chemistry. *Chemical reviews* **1995,** *95* (1), 25-48.
609 13. Begg, J. D.; Zavarin, M.; Tumey, S. J.; Kersting, A. B., Plutonium sorption and
610 desorption behavior on bentonite. *Journal of Environmental Radioactivity* **2015,** *141*, 106-114.
611 14. Powell, B. A.; Dai, Z. R.; Zavarin, M.; Zhao, P. H.; Kersting, A. B., Stabilization of
612 plutonium nano-colloids by epitaxial distortion on mineral surfaces. *Environmental Science &*
613 *Technology* **2011,** *45* (7), 2698-2703.
614 15. Begg, J. D.; Zavarin, M.; Zhao, P.; Tumey, S. J.; Powell, B.; Kersting, A. B., Pu(V)
615 and Pu(IV) Sorption to Montmorillonite. *Environmental Science & Technology* **2013,** *47* (10),
616 5146-5153.
617 16. Hixon, A. E.; Hu, Y. J.; Kaplan, D. I.; Kukkadapu, R. K.; Nitsche, H.; Qafoku, O.;
618 Powell, B. A., Influence of iron redox transformations on plutonium sorption to sediments.
619 *Radiochimica Acta* **2010,** *98* (9-11), 685-692.

17. Kirsch, R.; Fellhauer, D.; Altmaier, M.; Neck, V.; Rossberg, A.; Fanghanel, T.; Charlet, L.; Scheinost, A. C., Oxidation state and local structure of plutonium reacted with magnetite, mackinawite, and chukanovite. *Environmental Science & Technology* **2011,** *45* (17), 7267-7274.
18. Shaughnessy, D. A.; Nitsche, H.; Booth, C. H.; Shuh, D. K.; Waychunas, G. A.; Wilson, R. E.; Gill, H.; Cantrell, K. J.; Serne, R. J., Molecular interfacial reactions between Pu(VI) and manganese oxide minerals manganite and hausmannite. *Environmental Science & Technology* **2003,** *37* (15), 3367-3374.
19. Sanchez, A. L.; Murray, J. W.; Sibley, T. H., The Adsorption of Plutonium-Iv and Plutonium-V on Goethite. *Geochimica Et Cosmochimica Acta* **1985,** *49* (11), 2297-2307.
20. Zhao, P. H.; Begg, J. D.; Zavarin, M.; Tumey, S. J.; Williams, R.; Dai, Z. R. R.; Kips, R.; Kersting, A. B., Plutonium(IV) and (V) Sorption to Goethite at Sub-Femtomolar to Micromolar Concentrations: Redox Transformations and Surface Precipitation. *Environmental Science & Technology* **2016,** *50* (13), 6948-6956.
21. Romanchuk, A. Y.; Kalmykov, S. N.; Aliev, R. A., Plutonium sorption onto hematite colloids at femto- and nanomolar concentrations. *Radiochimica Acta* **2011,** *99* (3), 137-144.
22. Marshall, T. A.; Morris, K.; Law, G. T. W.; Livens, F. R.; Mosselmans, J. F. W.; Bots, P.; Shaw, S., Incorporation of Uranium into Hematite during Crystallization from Ferrihydrite. *Environmental Science & Technology* **2014,** *48* (7), 3724-3731.
23. Ferris, F. G.; Hallberg, R. O.; Lyven, B.; Pedersen, K., Retention of strontium, cesium, lead and uranium by bacterial iron oxides from a subterranean environment. *Applied Geochemistry* **2000,** *15* (7), 1035-1042.
24. Daisy, R. Accumulation and mobility of radionuclides in the Sellafield Near Shore. 2013.
25. Alberts, J. J.; Halverson, J. E.; Orlandini, K. A., The Distribution of Plutonium, Americium and Curium Isotopes in Pond and Stream Sediments of the Savannah River Plant, South-Carolina, USA. *Journal of Environmental Radioactivity* **1986,** *3* (4), 249-271.
26. Pinder, J. E.; Alberts, J. J.; Bowling, J. W.; Nelson, D. M.; Orlandini, K. A., The annual cycle of plutonium in the water column of a warm, monomictic reservoir. *Journal of Environmental Radioactivity* **1992,** *17* (1), 59-81.
27. Whicker, F. W.; Pinder, J. E.; Bowling, J. W.; Alberts, J. J.; Brisbin, I. L., DISTRIBUTION OF LONG-LIVED RADIONUCLIDES IN AN ABANDONED REACTOR COOLING RESERVOIR. *Ecol. Monogr.* **1990,** *60* (4), 471-496.
28. Benner, S. G.; Hansel, C. M.; Wielinga, B. W.; Barber, T. M.; Fendorf, S., Reductive dissolution and biomineralization of iron hydroxide under dynamic flow conditions. *Environmental Science & Technology* **2002,** *36* (8), 1705-1711.
29. Luther, G. W.; Kostka, J. E.; Church, T. M.; Sulzberger, B.; Stumm, W., Seasonal Iron Cycling in the Salt-Marsh Sedimentary Environment - the Importance of Ligand Complexes with Fe(Ii) and Fe(Iii) in the Dissolution of Fe(Iii) Minerals and Pyrite, Respectively. *Mar Chem* **1992,** *40* (1-2), 81-103.
30. King, F., 13 - Nuclear waste canister materials: Corrosion behavior and long-term performance in geological repository systems. In *Geological Repository Systems for Safe Disposal of Spent Nuclear Fuels and Radioactive Waste (Second Edition)*, Apted, M. J.; Ahn, J., Eds. Woodhead Publishing: 2017; pp 365-408.
31. Feron, D.; Crusset, D.; Gras, J. M., Corrosion issues in nuclear waste disposal. *Journal of Nuclear Materials* **2008,** *379* (1-3), 16-23.

32. Music, S.; Gotic, M.; Popovic, S., X-RAY-DIFFRACTION AND FOURIER-TRANSFORM INFRARED-ANALYSIS OF THE RUST FORMED BY CORROSION OF STEEL IN AQUEOUS-SOLUTIONS. *Journal of Materials Science* **1993,** *28* (21), 5744-5752.
33. El Hajj, H.; Abdelouas, A.; El Mendili, Y.; Karakurt, G.; Grambow, B.; Martin, C., Corrosion of carbon steel under sequential aerobic-anaerobic environmental conditions. *Corrosion Science* **2013,** *76*, 432-440.
34. Wersin, P.; Jenni, A.; Mader, U. K., Interaction of Corroding Iron with Bentonite in the Abm1 Experiment at Aspo, Sweden: A Microscopic Approach. *Clays and Clay Minerals* **2015,** *63* (1-2), 51-68.
35. Michel, F. M.; Ehm, L.; Antao, S. M.; Lee, P. L.; Chupas, P. J.; Liu, G.; Strongin, D. R.; Schoonen, M. A. A.; Phillips, B. L.; Parise, J. B., The Structure of Ferrihydrite, a Nanocrystalline Material. *Science* **2007,** *316* (5832), 1726-1729.
36. Fischer, W. R.; Schwertmann, U., FORMATION OF HEMATITE FROM AMORPHOUS IRON(III)HYDROXIDE. *Clays and Clay Minerals* **1975,** *23* (1), 33-&.
37. Combes, J. M.; Manceau, A.; Calas, G., FORMATION OF FERRIC OXIDES FROM AQUEOUS-SOLUTIONS - A POLYHEDRAL APPROACH BY X-RAY ABSORPTION-SPECTROSCOPY .2. HEMATITE FORMATION FROM FERRIC GELS. *Geochimica Et Cosmochimica Acta* **1990,** *54* (4), 1083-1091.
38. Schwertmann, U.; Cornell, R. M., Iron oxides in the laboratory. In *Iron Oxides in the Laboratory*, Wiley-VCH Verlag GmbH: 2000; pp i-xviii.
39. Das, S.; Hendry, M. J.; Essilfie-Dughan, J., Transformation of Two-Line Ferrihydrite to Goethite and Hematite as a Function of pH and Temperature. *Environmental Science & Technology* **2011,** *45* (1), 268-275.
40. Yang, R.; Tao, J.; Huang, Q.; Tie, B.; Lei, M.; Yang, Y.; Du, H., Co-adsorption of Cd(II) and Sb(III) by ferrihydrite: a combined XPS and ITC study. *Journal of Soils and Sediments* **2019,** *19* (3), 1319-1327.
41. Dyer, J. A.; Trivedi, P.; Scrivner, N. C.; Sparks, D. L., Lead Sorption onto Ferrihydrite. 2. Surface Complexation Modeling. *Environmental Science & Technology* **2003,** *37* (5), 915-922.
42. Jain, A.; Loeppert, R. H., Effect of Competing Anions on the Adsorption of Arsenate and Arsenite by Ferrihydrite. *Journal of Environmental Quality* **2000,** *29*, 1422-1430.
43. Smith, K. F.; Morris, K.; Law, G. T. W.; Winstanley, E. H.; Livens, F. R.; Weatherill, J. S.; Abrahamsen-Mills, L. G.; Bryan, N. D.; Mosselmans, J. F. W.; Cibin, G.; Parry, S.; Blackham, R.; Law, K. A.; Shaw, S., Plutonium(IV) Sorption during Ferrihydrite Nanoparticle Formation. *ACS Earth and Space Chemistry* **2019**.
44. Bots, P.; Shaw, S.; Law, G. T. W.; Marshall, T. A.; Mosselmans, J. F. W.; Morris, K., Controls on the Fate and Speciation of Np(V) During Iron (Oxyhydr)oxide Crystallization. *Environmental Science & Technology* **2016,** *50* (7), 3382-3390.
45. Um, W.; Serne, R. J.; Brown, C. F.; Rod, K. A., Uranium(VI) sorption on iron oxides in Hanford Site sediment: Application of a surface complexation model. *Applied Geochemistry* **2008,** *23* (9), 2649-2657.
46. Romanchuk, A. Y.; Gusev, I. V.; Vlasova, I. E.; Petrov, V. G.; Kuzmenkova, N. V.; Egorova, B. V.; Zakharova, E. V.; Volkova, A. G.; Kalmykov, S. N., Interaction of Plutonium with Iron- and Chromium-Containing Precipitates under the Conditions of Reservoir Bed for Liquid Radioactive Waste. *Radiochemistry* **2016,** *58* (6), 662-667.

47. Sylvester, P.; Milner, T.; Jensen, J., Radioactive liquid waste treatment at Fukushima Daiichi. *Journal of Chemical Technology and Biotechnology* **2013,** *88* (9), 1592-1596.
48. Winstanley, E. H.; Morris, K.; Abrahamsen-Mills, L. G.; Blackham, R.; Shaw, S., U(VI) sorption during ferrihydrite formation: Underpinning radioactive effluent treatment. *Journal of Hazardous Materials* **2019,** *366*, 98-104.
49. McBriarty, M. E.; Soltis, J. A.; Kerisit, S.; Qafoku, O.; Bowden, M. E.; Bylaska, E. J.; De Yoreo, J. J.; Ilton, E. S., Trace Uranium Partitioning in a Multiphase Nano-FeOOH System. *Environmental Science & Technology* **2017,** *51* (9), 4970-4977.
50. Zavarin, M.; Zhao, P.; Dai, Z.; Kersting Annie , B., Plutonium sorption and precipitation in the presence of goethite at 25 and 80 ○C. In *Radiochimica Acta*, 2014; Vol. 102, p 983.
51. Felmy, A. R.; Moore, D. A.; Qafoku, O.; Buck, E.; Conradson, S. D.; Ilton, E. S., Heterogeneous reduction of (PuO2)-Pu-239 by aqueous Fe(II) in the presence of hematite. *Radiochimica Acta* **2013,** *101* (11), 701-710.
52. Powell, B. A.; Dai, Z.; Zavarin, M.; Zhao, P.; Kersting, A. B., Stabilization of Plutonium Nano-Colloids by Epitaxial Distortion on Mineral Surfaces. *Environmental Science & Technology* **2011,** *45* (7), 2698-2703.
53. Dumas, T.; Fellhauer, D.; Schild, D.; Gaona, X.; Altmaier, M.; Scheinost, A. C., Plutonium Retention Mechanisms by Magnetite under Anoxic Conditions: Entrapment versus Sorption. *Acs Earth and Space Chemistry* **2019,** *3* (10), 2197-2206.
54. Joseph, C.; Balboni, E.; Baumer, T.; Treinen, K.; Kersting, A. B.; Zavarin, M., Plutonium Desorption from Nuclear Melt Glass-Derived Colloids and Implications for Migration at the Nevada National Security Site, USA. *Environmental Science & Technology* **2019,** *53* (21), 12238-12246.
55. Novikov, A. P.; Kalmykov, S. N.; Utsunomiya, S.; Ewing, R. C.; Horreard, F.; Merkulov, A.; Clark, S. B.; Tkachev, V. V.; Myasoedov, B. F., Colloid transport of plutonium in the far-field of the Mayak Production Association, Russia. *Science* **2006,** *314* (5799), 638-641.
56. Batuk, O. N.; Conradson, S. D.; Aleksandrova, O. N.; Boukhalfa, H.; Burakov, B. E.; Clark, D. L.; Czerwinski, K. R.; Felmy, A. R.; Lezama-Pacheco, J. S.; Kalmykov, S. N.; Moore, D. A.; Myasoedov, B. F.; Reed, D. T.; Reilly, D. D.; Roback, R. C.; Vlasova, I. E.; Webb, S. M.; Wilkerson, M. P., Multiscale Speciation of U and Pu at Chernobyl, Hanford, Los Alamos, McGuire AFB, Mayak, and Rocky Flats. *Environmental Science & Technology* **2015,** *49* (11), 6474-6484.
57. Lukashenko, S.; Kabdyrakova, A.; Lind, O. C.; Gorlachev, I.; Kunduzbayeva, A.; Kvochkina, T.; Janssens, K.; De Nolf, W.; Yakovenko, Y.; Salbu, B., Radioactive particles released from different sources in the Semipalatinsk Test Site. *Journal of Environmental Radioactivity* **2020,** *216*.
58. Joshi, S. R., LANTHANUM FLUORIDE COPRECIPITATION TECHNIQUE FOR THE PREPARATION OF ACTINIDES FOR ALPHA-PARTICLE SPECTROMETRY. *Journal of Radioanalytical and Nuclear Chemistry* **1985,** *90* (2), 409-414.
59. Hayes, T. M.; Boyce, J. B., Extended X-Ray Absorption Fine Structure Spectroscopy. In *Solid State Physics*, Ehrenreich, H.; Seitz, F.; Turnbull, D., Eds. Academic Press: 1983; Vol. 37, pp 173-351.
60. Booth, C. H. *RSXAP EXAFS Analysis Package*.
61. Li, G. G.; Bridges, F.; Booth, C. H., X-RAY-ABSORPTION FINE-STRUCTURE STANDARDS - A COMPARISON OF EXPERIMENT AND THEORY. *Physical Review B* **1995,** *52* (9), 6332-6348.

62. Ankudinov, A. L.; Ravel, B.; Rehr, J. J.; Conradson, S. D., Real-space multiple-scattering calculation and interpretation of x-ray-absorption near-edge structure. *Physical Review B* **1998,** *58* (12), 7565-7576.

63. Booth, C. H.; Hu, Y. J. In *Confirmation of standard error analysis techniques applied to EXAFS using simulations*, 14th International Conference on X-Ray Absorption Fine Structure (XAFS14), Camerino, ITALY, Jul 26-31; Iop Publishing Ltd: Camerino, ITALY, 2009.

64. G, W. R. W., Interscience Publishers, New York: 1963.

65. Wylie, E. M.; Olive, D. T.; Powell, B. A., Effects of Titanium Doping in Titanomagnetite on Neptunium Sorption and Speciation. *Environmental Science & Technology* **2016,** *50* (4), 1853-1858.

66. Romanchuk, A. Y.; Kalmykov, S. N.; Egorov, A. V.; Zubavichus, Y. V.; Shiryaev, A. A.; Batuk, O. N.; Conradson, S. D.; Pankratov, D. A.; Presnyakov, I. A., Formation of crystalline PuO2+x center dot nH(2)O nanoparticles upon sorption of Pu(V,VI) onto hematite. *Geochimica Et Cosmochimica Acta* **2013,** *121*, 29-40.

67. Hu, Y.-J.; Kestrel Schwaiger, L.; Booth Corwin, H.; Kukkadapu Ravi, K.; Cristiano, E.; Kaplan, D.; Nitsche, H., Molecular interactions of plutonium(VI) with synthetic manganese-substituted goethite. In *Radiochimica Acta International journal for chemical aspects of nuclear science and technology*, 2010; Vol. 98, p 655.

68. Bargar, J. R.; Reitmeyer, R.; Lenhart, J. J.; Davis, J. A., Characterization of U(VI)-carbonato ternary complexes on hematite: EXAFS and electrophoretic mobility measurements. *Geochimica Et Cosmochimica Acta* **2000,** *64* (16), 2737-2749.

69. Seco, F.; Hennig, C.; de Pablo, J.; Rovira, M.; Rojo, I.; Marti, V.; Gimenez, J.; Duro, L.; Grive, M.; Bruno, J., Sorption of Th(IV) onto Iron Corrosion Products: EXAFS Study. *Environmental Science & Technology* **2009,** *43* (8), 2825-2830.

70. Dumas, T.; Guigue, M.; Moisy, P.; Colina-Ruiz, R.; de Leon, J. M.; Matara-Aho, M.; Solari, P. L.; Monfort, M.; Moulin, C.; Beccia, M. R.; Den Auwer, C., Experimental Speciation of Plutonium(IV) in Natural Seawater. *Chemistryselect* **2018,** *3* (7), 2021-2024.

71. Calvin, S.; Riedel, C. J.; Carpenter, E. E.; Morrison, S. A.; Stroud, R. M.; Harris, V. G., Estimating crystallite size in polydispersed samples using EXAFS. *Physica Scripta* **2005,** *T115*, 744-748.

72. Shannon, R. D., Revised Effective Ionic-Radii and Systematic Studies of Interatomic Distances in Halides and Chalcogenides. *Acta Crystallographica Section A* **1976,** *32* (Sep1), 751-767.

73. Wang, X.; Zhu, M.; Koopal, L. K.; Li, W.; Xu, W.; Liu, F.; Zhang, J.; Liu, Q.; Feng, X.; Sparks, D. L., Effects of crystallite size on the structure and magnetism of ferrihydrite. *Environmental Science: Nano* **2016,** *3* (1), 190-202.

74. Siroux, B.; Beaucaire, C.; Tabarant, M.; Benedetti, M. F.; Reiller, P. E., Adsorption of strontium and caesium onto an Na-MX80 bentonite: Experiments and building of a coherent thermodynamic modelling. *Applied Geochemistry* **2017,** *87* (Supplement C), 167-175.

75. Vila, F. D.; Rehr, J. J.; Rossner, H. H.; Krappe, H. J., Theoretical x-ray absorption Debye-Waller factors. *Physical Review B* **2007,** *76* (1).

76. Chase, M. W.; Jr, n.; Downey, J. R.; Jr, n.; McDonald, R. A.; Syverud, A. N., *J. Phys. Chem. Ref. Data* **1985,** *14 (Suppl. 1*, 1.

77. Kaur, N.; Grafe, M.; Singh, B.; Kennedy, B., SIMULTANEOUS INCORPORATION OF Cr, Zn, Cd, AND Pb IN THE GOETHITE STRUCTURE. *Clays and Clay Minerals* **2009,** *57* (2), 234-250.

802 78. Kersting, A. B.; Efurd, D. W.; Finnegan, D. L.; Rokop, D. J.; Smith, D. K.; Thompson,
803 J. L., Migration of plutonium in ground water at the Nevada Test Site. *Nature* **1999,** *397* (6714),
804 56-59.
805 79. Toropov, A. S., Migration Forms of Anthropogenic Radionuclides in Tunnel Waters at
806 the Degelen Mountains, Semipalatinsk Test Site. *Geochemistry International* **2020,** *58* (3), 342-
807 351.
808 80. Berner, U. R., Evolution of pore water chemistry during degradation of cement in a
809 radioactive waste repository environment. *Waste Management* **1992,** *12* (2), 201-219.
810 81. Wallace, S. H.; Shaw, S.; Morris, K.; Small, J. S.; Burke, I. T., Alteration of Sediments
811 by Hyperalkaline K-Rich Cement Leachate: Implications for Strontium Adsorption and
812 Incorporation. *Environmental Science & Technology* **2013,** *47* (8), 3694-3700.
813 82. Wallace, S. H.; Shaw, S.; Morris, K.; Small, J. S.; Fuller, A. J.; Burke, I. T., Effect of
814 groundwater pH and ionic strength on strontium sorption in aquifer sediments: Implications for
815 Sr-90 mobility at contaminated nuclear sites. *Applied Geochemistry* **2012,** *27* (8), 1482-1491.
816 83. Deng, Y.; Harsh, J. B.; Flury, M.; Young, J. S.; Boyle, J. S., Mineral formation during
817 simulated leaks of Hanford waste tanks. *Applied Geochemistry* **2006,** *21* (8), 1392-1409.

818

819

820